

Deep learning driven crop classification and chlorophyll content estimation for the Nexus food higher productions using multispectral remote sensing images

Karthikeyan B.¹, Mohan V.², Chamundeeswari G.^{3*}, and Ruba M.⁴

¹Department of Information Technology, Panimalar Engineering College, Chennai, India

²Department of ECE, Saranathan College of Engineering, Panjapur, Trichy-620012, India

³Saveetha School of Engineering, Saveetha Institute of Medical and Technical Sciences, Saveetha University, Thandalam, Chennai, 602105, India

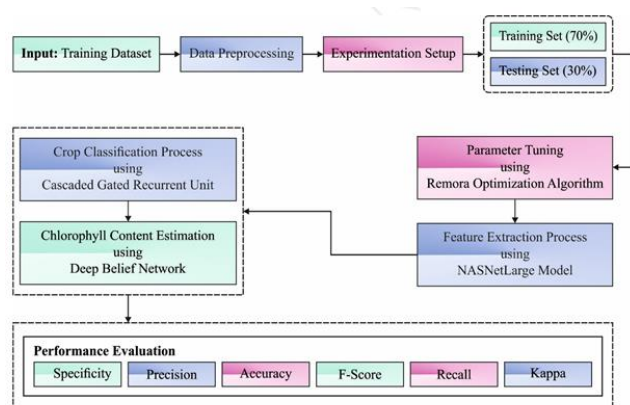
⁴CSE, K.Ramakrishnan College of Engineering, Trichy, India

Received: 11/11/2022, Accepted: 30/11/2022, Available online: 05/12/2022

*to whom all correspondence should be addressed: e-mail: chamundy2022@gmail.com

<https://doi.org/10.30955/gnj.004560>

Graphical abstract



Abstract

Due to the development of open access medium-high resolution remote sensing data like multispectral remote sensing images, crop classification becomes a hot research topic to be realized on large scale using machine learning (ML) models. At the same time, chlorophyll content is a critical index used for defining crop growth conditions, photosynthetic ability, and physiological position. It has an adaptive characteristic which finds useful to monitor crop growth conditions and understand the procedure of material and energy exchange among crops and the environment. Recently, several research works have been carried out to estimate chlorophyll content on multispectral remote sensing images. The recent advances in deep learning models enable us to effectively classify different crop types and estimate chlorophyll content on multispectral remote sensing images. In this view, this paper presents a new remora optimization with deep learning driven crop classification and chlorophyll content estimation (RODLD-C4E) model using multispectral remote sensing images. The proposed RODLD-C4E model

intends to properly identify the crop type and chlorophyll content. For accomplishing this, the proposed RODLD-C4E model initially derives a RO algorithm with NASNetLarge model for feature extraction process. The utilization of RO algorithm enables to effectually adjust the hyperparameters of the NasNetLarge model. Besides, cascaded gated recurrent unit (CGRU) model is employed for crop type classification. Finally, deep belief network (DBN) model is applied to estimate the chlorophyll content exist in the crop. To demonstrate the better performance of RODLD-C4E model, a wide ranging experimental analysis was implemented on benchmark dataset. The comparative analysis pointed out the better outcomes of the RODLD-C4E model under several aspects.

Keywords: Multispectral remote sensing images, agriculture, crop classification, chlorophyll content estimation, deep learning, parameter tuning

1. Introduction

Agriculture is the science or process of manufacturing and harvesting crops systematically. Growth in agricultural crops nowadays becomes essential because of restrictions in the development of land and continuously rising demand for food (Senthilnath *et al.*, 2016). Agricultural production is termed as the product of crop yield and planting region and therefore production valuation contains yield estimation and area prediction. Thus, there exists a vigorous demand for making the maximum utilization of existing sources for cultivation process (Townsend *et al.*, 2001). The utilization of remote sensing contains numerous benefits and applications, and major application among them is crop classification; i.e., distinguishing amongst distinct types of crops (Rußwurm *et al.*, 2017). Satellite images could also be considered feasible sources for examining the temporary variations in the agricultural actions of a specific region (Garnot *et al.*, 2019). The development of crops from sowing to

harvesting could be observed by such satellite images. The georeferenced and orthorectified satellite images could be utilized for finding problematical zones and the size of the zone affected (Moriarty *et al.*, 2019).

Monitoring the usage of agricultural land is of critical significance for ensuring the continued health of food production, biodiversity, and forest ecosystems. A combination of factors, including a warming climate, shifting eating patterns, and an expanding global population, are putting pressure on land that has not yet been farmed while simultaneously driving up production levels in places that are already farmed. The spread of cropland and the intense use of agricultural land are often linked to negative ecological consequences such as the destruction of forests and the loss of biodiversity, as well as the deterioration of ecosystem services such as the quality of ground and surface water. As a result, thorough and accurate monitoring of agricultural lands is an absolutely necessary component in the achievement of optimum and sustainable management of these areas. The knowledge of agricultural regions and particular land uses is essential for many political initiatives that try to lessen and relieve the negative effects that intensive agriculture has on the surrounding environment. Incentives that are driven by policy, for instance, encourage a specified percentage of a farm area to remain intensively utilised grassland in order to preserve biodiversity. Similarly, subsidies are given to encourage a particular crop mix to be rotated in a farm's cycle of crops. The collection of data has historically relied on the self-reporting of farmers and the spot monitoring of their operations by authorities in the field. This method of data collection is arduous, expensive, and prone to inaccuracies. Combining the most up-to-date machine learning techniques with satellite data that is freely accessible to the public opens up a world of new opportunities for accurate, spatially dense monitoring of agricultural areas that is also characterised by high temporal resolution and cheap cost. Researchers are presently relying on approaches that use deep learning in order to do crop categorization.

Multi-spectral satellite images enable classification and recognition of crops, it takes into account the variations in reflectance as a function of the specific yield types (Li *et al.*, 2019). Crop classification discovers applications in checking and planning efficient crop cultivation, soil and water quality studies, and land usage. But owing to the variations in cultivation of crops inside a geographic region, the procedure of classification becomes a significant problem (Thyagarajan *et al.*, 2019). Primary productivity and respiration are closely linked to the biochemical and biophysical variables of the vegetation. Amongst these variables, chlorophyll is a critical antenna pigment that is accountable for absorbing light and transferring it in photosynthesis. Variations in the leaf chlorophyll content (LCC) therefore straight forwardly influence biochemical functions namely primary production and photosynthesis (Moody *et al.*, 2017). Thus, quantitative examination of LCC has important consequences, not for sensing the procedure of material

and energy exchange amongst the environment and plants, as well as for observing, nutritional status, stress conditions, and crop growth in agricultural applications.

In recent times, deep learning (DL) was broadly utilized and is considered mainstream in artificial intelligence and machine learning (ML) (Kumar *et al.*, 2021). DL is representation learning methodology which mechanically studies internal characteristics representation with various levels from novel images instead of empirical feature models, and has proved to be more proficient in image classification and object identification (Yang *et al.*, 2021). By contrast, vegetation indexes namely NDVI utilize various bands and might result in low outcomes in hard circumstances, e.g., crop classification where the geometry, periods, spectrums, and the interaction of several kinds of crops must be assumed. While novel temporary images utilized as feature input could comprise noises or unfavourable data which diminish the outcome of a classifier.

This paper presents a new remora optimization with deep learning driven crop classification and chlorophyll content estimation (RODLD-C4E) model using multispectral remote sensing images. The proposed RODLD-C4E model derives a RO algorithm with NASNetLarge model for feature extraction process. The use of RO algorithm allows for effectively changing the hyperparameters of the NasNetLarge model. Also, cascaded gated recurrent unit (CGRU) model is employed for crop type classification. Lastly, deep belief network (DBN) model is applied to estimate the chlorophyll content that exists in the crop. To demonstrate the better performance of RODLD-C4E model, a wide ranging experimental analysis is performed on benchmark dataset.

2. Related works

Denis *et al.* (2020) measured how spatial remote sensing might assist the process of organic crop certification by rising a methodology that allows certification body target to priority in situ control crop field stated as organic however that display on satellite images a closer appearance to traditional fields. Therefore, the capability of multi-spectral satellite images to distinguish among conventional maize and organic fields was evaluated by using four groups of satellite images of spectral and spatial resolutions attained at various development stages of crop over a considerable amount of maize field. Singhal *et al.* (2019) attempt has been made to estimate the leaf chlorophyll concentration of standing maize plants in higher resolution (5 cm) multispectral Unmanned Aerial Vehicle (UAV) imagery. Then, estimated ML algorithm is integrated with spectral dataset and ground truth chlorophyll for modelling the chlorophyll estimations.

Brewer *et al.* (2022) estimated the efficacy of multi-spectral UAV images with the random forest machine learning technique for estimating the chlorophyll content of maize via different development stages. The result shows that the red-edge and near-infrared wavelength bands and vegetation indices derived from the wavelength are needed to estimate chlorophyll content under the maize phenotyping (Singhal *et al.*, 2019).

estimated the ML approach kernel ridge regression integrated with spectral dataset and ground-truth chlorophyll dataset for modelling the chlorophyll estimates. Also, the multivariate analysis was employed on spectroradiometer and UAV dataset that suggested red band for predicting chlorophyll content with R2 value larger than 0.6. Wang *et al.* (2022) enable the transfer of classification models over years and regions for Gaofen PMS (2-m resolution) and Sentinel-2A (10-m resolution) images. The feature selection (FS) based prediction using UNet++ framework and up-sampling of minor class demonstrates the abilities of DL generalization to classify complicated ground objects that provide better results. Zhou *et al.* (2018) the classification method of CNN and SVM is compared to extract the spatial distribution of crop planting region in Sentinel-2A multispectral remote sensing images in China.

Ma *et al.* (2021) examined the classifier potential of multi-spectral classifier method to farmland with planting infrastructures of several complexities. UAV-RS technology are utilized for obtaining multi-spectral image of 3 analysis regions with low-, medium-, and high-complexity planting infrastructures comprising 3, 5, and 8 kinds of crops correspondingly. Recursive feature elimination was used to choose feature subsets for three analysis zones (RFE). The three areas of analysis have now been incorporated into OB-RF and OB-SVM classifier algorithms. By deleting satellite data at the pixel level, analyzing every available band, and dispersing its data across time, Siesto *et al.* (2021) introduced an innovative approach that creates synthetic images. Images from Sentinel-2 were used to create a deep convolutional network model that can distinguish between different crops a year after being trained on data from prior years. According to Qi *et al.* (2021) two peanut types, Yanghua 1 and Yueyou 45 are planted at varied densities, with 8 vegetation indices calculated using multi-spectral drone imagery. For the 1D linear regression techniques of NDVI and GNDVI (Green NDVI), as well as the MLR methodology, a far higher degree of set-up and precision was necessary than for the other indices. When testing for chlorophyll concentration in peanuts, BPNN is a better option than the RF approach for ensuring optimal fit and accuracy. It was determined by Denis *et al.* (2021) that satellite remote sensing might help the certification process for organic crop fields that look to be more traditional on satellite images but are certified as organic by the certification agency. Therefore, the capability of multi-spectral satellite images to distinguish among conventional maize and organic fields was evaluated by using four groups of satellite images of spectral and spatial resolutions attained at various development stages of crop over a considerable amount of maize field.

3. The proposed model

In this study, a new RODLD-C4E model has been developed to properly identify the crop type and chlorophyll content. The proposed RODLD-C4E model initially derives a RO algorithm with NASNetLarge model for feature extraction process. In addition, the CGRU model is employed for crop type classification. At last, the

DBN model is applied to estimate the chlorophyll content that exists in the crop. Figure 1 demonstrates the overall process of RODLD-C4E technique.

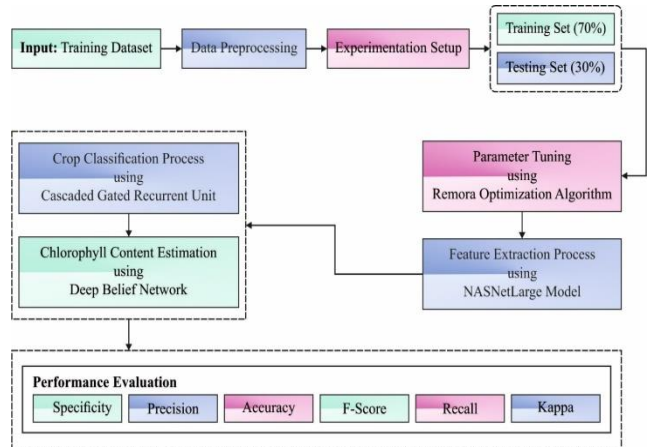


Figure 1. Overall process of RODLD-C4E technique

3.1. Feature extraction

The initial stage of crop classification is to produce a useful set of features by the NASNetLarge model. Neural architecture search (NAS) is the search technique that needs to be deployed. Child networks with different frameworks is sampled by a controller RNN in NAS. Child network is taught to accomplish some accuracy on a validation set i.e., held out for convergence. The resultant accuracy value is utilized for upgrading the controller that sequentially generates accurate architecture over time. The policy gradient is utilized for upgrading the controller weight. According to the realization that architecture engineered with CNN generally uncover recurrent pattern that includes the combination of convolution filter bank and nonlinearity along with a careful selection of connection, the NasNet searching space has been made (for instance, the repeated module in the ResNet and inception modules) (Ünal *et al.*, 2022). The finding suggests that the controller RNN might be capable of predicting a generic convolution cell. For accommodating input of spatial dimension and depth of filtering, this cell can be stacked sequentially. In this technique, the convolution net overall design is manually predefined. They are composed of convolution cell that has similar shape as the original however they are differently weighted. Two kinds of convolution cells are utilized for rapidly developing scalable architecture for images of any size: (1) convolution cell returns a feature map with a two-fold reduction in width and height, and (2) convolution cell produces a feature map with equal dimensions.

In this work, the RO algorithm enables to effectually adjust the hyperparameters of the NasNetLarge model. The position updating process of RO algorithm is modelled on the basis of the algorithm elite notion, given in the following.

$$R_i^{t+1} = R_{best}^t - \left(rand \times \left(\frac{R_{best}^t - R_{rand}^t}{2} \right) - R_{rand}^t \right) \quad (1)$$

Now, R_{rand}^t denotes a random location. To estimate whether or not it is essential to replace the host, they

should frequently take modest steps around the host, similar to the knowledge development. The equation for modelling the abovementioned principle is given below:

$$R_{att} = R_i^t - (R_i^t - R_{pre}) \times rand \quad (2)$$

Here R_{pre} indicates the location of the preceding iteration, and R_{att} represent a tentative step. The estimation of the fitness function (FF) of the attempted solution $f(R_{att})$ and the existing solution $f(R_i^t)$ is defined by the decision of this step. For instance, while resolving the problems, when the FF value generated by the presented solution is lesser when compared to the existing solution,

$$f(R_i^t) > f(R_{att}) \quad (3)$$

Remora selects various methodologies for local optimal, as follows. Its return to host selecting when the FF value of attempted solutions is higher than the current solution.

$$f(R_i^t) < f(R_{att}) \quad (4)$$

The position upgrade equation of Remora related to the whale was recovered by the original WOA method, as follows:

$$R_{i+1} = D \times e^{\alpha} \times \cos(2\pi\alpha) + R_i \quad (5)$$

$$\alpha = rand \times (a - 1) + 1 \quad (6)$$

$$a = -\left(1 + \frac{t}{T}\right) \quad (7)$$

$$D = |R_{best} - R_i| \quad (8)$$

The location is regarded as the same once a Remora is on a whale in the broader solution space. D indicates the space amongst the hunter and prey α represents an arbitrary number within $[-1, 1]$, and a indicates a value that exponentially reduces from $[-2, -1]$. Further, The exploitation process is divided into host feeding (Jia *et al.*, 2021). Now, the optimum solution is condensed to the host location. The mathematical expression of the abovementioned process is given below:

$$R_i^t = R_i^t + A \quad (9)$$

$$A = B \times (R_i^t - C \times R_{best}) \quad (10)$$

$$B = 2 \times V \times rand - V \quad (11)$$

$$V = 2 \times \left(1 - \frac{t}{T}\right) \quad (12)$$

3.2. Crop classification module

For crop classification process, the CGRU model has been employed to it. A GRU is a new memory cell that has proved efficient performance in different applications. It is considered to be an improvement and simplification of LSTM and comparative performance to LSTM (Xu *et al.*, 2018). To clearly define a GRU, we concisely present LSTM. In RNN, the hidden unit is the main element since it is accountable for forgetting or remembering certain data. The LSTM is being implemented properly and has better variant.

$$\begin{cases} f_t = \sigma(W_{xf}x_t + W_{hf}h_{t-1} + W_{cf}C_{t-1}) \\ i_t = \sigma(W_{xi}x_t + W_{hi}h_{t-1} + W_{ci}C_{t-1}) \\ C_t = f_t \odot C_{t-1} + i_t \odot \tanh(W_{xc}x_t + W_{hc}h_{t-1}) \\ O_t = \sigma(W_{xo}x_t + W_{ho}h_{t-1} + W_{co}C_{t-1}) \\ h_t = O_t \odot \tanh(C_t) \end{cases} \quad (13)$$

Here, x indicates the input vector, C denotes the cell state and h represents the output vector. σ denotes a sigmoid function, \odot implies the Hadamard product and W signifies undefined parameter. t signifies the present time and $t - 1$ represents the last time. Where i represents the input gate that decides what data need to be saved in the cell state. f represent the forget gate that decides what data need to be eliminated from the cell state. O indicates the output gate that decides what data to output. In contrast to LSTM, a GRU comprises certain simplification.

$$\begin{cases} r_t = \sigma(W_r x_t + U_r h_{t-1}) \\ z_t = \sigma(W_z x_t + U_z h_{t-1}) \\ \tilde{h}_t = \tanh(W_h x_t + U(h_t \odot h_{t-1})) \\ h_t = (1 - z_t)h_{t-1} + z_t \tilde{h}_t \end{cases} \quad (14)$$

Therefore, the GRU has fewer parameters and is very simple when compared to the LSTM architecture providing greater benefits interms of convergence and performance. In succeeding experiments, GRU shows an enormous benefit. In CGRU model, a set of GRU units is cascaded together to enhance results.

3.3. Chlorophyll Content Estimation Module

Finally, the DBN model is applied to estimate the chlorophyll content that exists in the crop. A typical DBN is stacked by using RBM that is special form of Markov random field (Li *et al.*, 2019). It comprises of single visible layer, that is defined by $v = \{v_1, v_2, \dots, v_i, \dots, v_n\}^T$ ($v_i \in \{0, 1\}$ single hidden layer is defined by $h = \{h_1, h_2, \dots, h_i, \dots, h_n\}^T$ ($h_i \in \{0, 1\}$). The visible layer is connected to the hidden layer via weight connection, and neuron of every layer isn't linked together:

$$E(v, h | \vartheta) = - \sum_{i=1}^n \sum_{j=1}^m v_i w_{ij} h_j - \sum_{i=1}^n a_i v_i - \sum_{j=1}^m b_j h_j \quad (15)$$

Whereas $\vartheta = \{w, a, b\}$, n , and m indicate the count of visible and hidden neurons, correspondingly. i and j

indicate the i th and j th neurons, v_i and h_j represents the i th visible neural and the j th hidden neurons, a_i and b_j represent the bias of i th visible neural and the j th hidden neural, and w_{ij} signifies the weight among i th visible neuron and j th hidden neuron. Figure 2 depicts the framework of DBN.

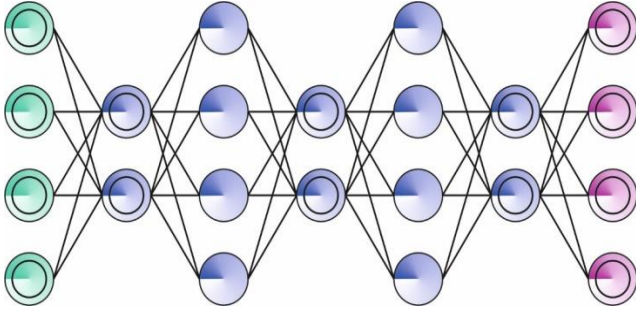


Figure 2. Structure of DBN

The joint possibility of visible neurons and the hidden neuron is shown in the following equation:

$$P(v, h | \vartheta) = \frac{1}{Z(\vartheta)} \exp(-E(v, h | \vartheta)) \quad (16)$$

that is Gibbs distribution of the RBM. $Z(\vartheta)$ indicates the partition function and is described in the following:

$$Z(\vartheta) = \sum_v \sum_h \exp(-E(v, h | \vartheta)) \quad (17)$$

The two edge possibilities of visible and hidden neurons are determined by:

$$P(v) = \frac{1}{Z(\vartheta)} \sum_h \exp(-E(v, h | \vartheta)) \quad (18)$$

$$P(h) = \frac{1}{Z(\vartheta)} \sum_v \exp(-E(v, h | \vartheta)) \quad (19)$$

The conditional probability of the visible and hidden neurons are shown as follows:

$$P(v_i | h) = \prod_i P(v_i | h) \quad (20)$$

$$P(h_j | v) = \prod_j P(h_j | v) \quad (21)$$

The visible and hidden neurons are independent, hence the distribution of the conditional probability is described by:

$$P(v_i = 1 | h) = \frac{1}{1 + \exp(-a_i - \sum_{j=1}^m w_{ij} h_j)} \quad (22)$$

$$P(h_j = 1 | v) = \frac{1}{1 + \exp(-b_j - \sum_{i=1}^n w_{ij} v_i)} \quad (23)$$

The visible layer v_i signifies the input dataset, viz., mapped to the hidden state based on the probability in Eq. (23). Subsequently, this constitutes the first RBM. At the same time, it is the input dataset of the next RBM. Repeat this procedure for updating the parameter, to form a feature

depiction i.e., more abstract and representability when compared to the lower layer. The weight is upgraded as:

$$\Delta w_{ij} = \eta (\langle v_i h_j \rangle - \langle v_i \rangle \langle h_j \rangle) \quad (24)$$

Whereas $\eta \in (0, 1)$ indicates the learning rate, $\langle \cdot \rangle$ represents the mean over the training dataset.

4. Performance validation

The experimental validation of the RODLD-C4E model is tested using two benchmark datasets namely Indian Pines dataset and Salinas dataset. A few sample images are demonstrated in Figure 3. Table 1 depicts the described dataset details.

4.1. Simulation parameters

The performance of the proposed method was evaluated using the most modern methodologies available. The experimental operations were carried out with the assistance of Google co-laboratory and MATLAB R 2018b programming language. The study was carried out using a personal computer that had an Intel(R) Core(TM) i5-6500 processor operating at 3.20 ghz range and 8 GB of random access memory (RAM).

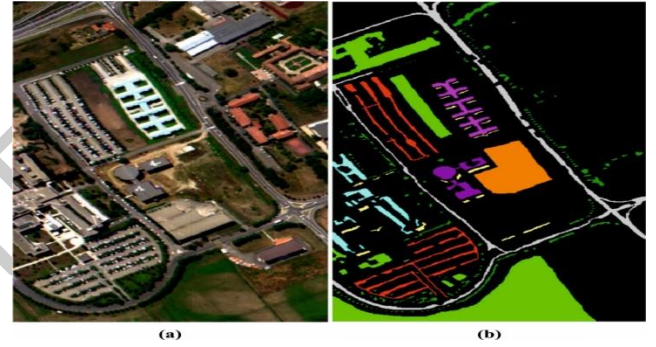


Figure 3. a) Remote Sensing Image b) Ground Truth Image

Table 1. Dataset details

Class Names	Number of Samples in Dataset	
	Indian Pine Dataset	Salinas Dataset
Category-01	36	1485
Category-02	1083	2793
Category-03	611	1462
Category-04	73	1051
Category-05	350	2007
Category-06	542	2982
Category-07	21	2649
Category-08	363	8445
Category-09	12	4667
Category-10	729	2465
Category-11	1829	805
Category-12	457	1434
Category-13	159	705
Category-14	954	832
Category-15	301	5462
Category-16	67	1354
Total No. of Samples	7587	40598

Figure 4 demonstrates the confusion matrix produced by the RODLD-C4E model on 30% of testing (TS) data on

Indian Pines dataset. The figure indicated that the RODLD-C4E model has proficiently recognized 16 classes.

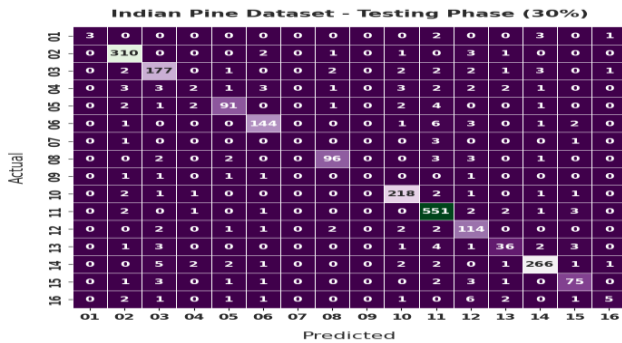


Figure 4. Confusion matrix of RODLD-C4E technique on 30% of TS data on Indian Pines dataset

Table 2. Result analysis of RODLD-C4E technique with several measures on Indian Pines dataset

Class Label	Accuracy	Precision	Recall	Specificity	F-Score
Category-01	99.74	100.00	33.33	100.00	50.00
Category-02	98.86	94.51	97.48	99.08	95.98
Category-03	98.33	88.94	91.71	98.94	90.31
Category-04	98.81	25.00	8.70	99.73	12.90
Category-05	98.99	90.10	87.50	99.54	88.78
Category-06	98.90	92.90	91.14	99.48	92.01
Category-07	99.78	0.00	0.00	100.00	0.00
Category-08	99.21	93.20	89.72	99.68	91.43
Category-09	99.78	0.00	0.00	100.00	0.00
Category-10	98.95	93.56	96.04	99.27	94.78
Category-11	97.98	94.19	97.87	98.02	95.99
Category-12	98.38	80.85	91.94	98.75	86.04
Category-13	98.90	78.26	70.59	99.55	74.23
Category-14	98.64	95.00	93.99	99.30	94.49
Category-15	98.95	86.21	86.21	99.45	86.21
Category-16	99.21	62.50	25.00	99.87	35.71
Average	98.96	73.45	66.33	99.42	68.05

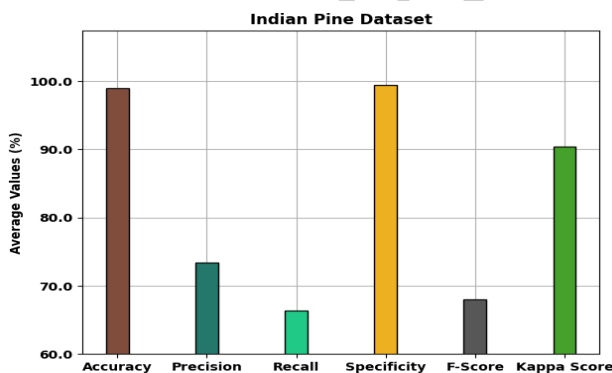


Figure 5. Result analysis of RODLD-C4E technique on Indian Pines dataset

The training accuracy (TA) and validation accuracy (VA) attained by the RODLD-C4E model on Indian Pines dataset is demonstrated in Figure 6. The experimental outcome implied that the RODLD-C4E model has gained maximum values of TA and VA. In specific, the VA seemed to be higher than TA.

Table 2 and Figure 5 offer a detailed discussion of the crop classification outcomes reported by the RODLD-C4E model on Indian Pines dataset. The experimental values indicated that the RODLD-C4E model has proficiently recognized all the class labels. For instance, with category 1, the RODLD-C4E model has provided $accu_y$, $prec_n$, $reca_i$, $spec_y$, and F_{score} of 99.74%, 100%, 33.33%, 100%, and 50% respectively. At the same time, with category 10, the RODLD-C4E model has provided $accu_y$, $prec_n$, $reca_i$, $spec_y$, and F_{score} of 98.95%, 93.56%, 96.04%, 99.27%, and 94.78% respectively. In line with, with category 16, the RODLD-C4E model has provided $accu_y$, $prec_n$, $reca_i$, $spec_y$, and F_{score} of 99.21%, 62.50%, 25%, 99.87%, and 35.71% respectively.

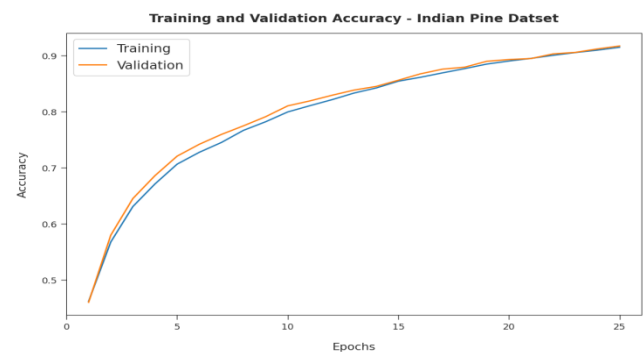


Figure 6. TA and VA analysis of RODLD-C4E technique on Indian Pines dataset

The training loss (TL) and validation loss (VL) achieved by the RODLD-C4E model on Indian Pines dataset are established in Figure 7. The experimental outcome inferred that the RODLD-C4E model has been able to achieve least values of TL and VL. In specific, the VL seemed to be lower than TL.

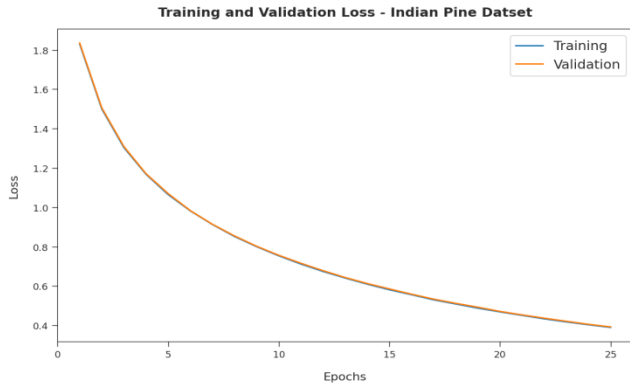


Figure 7. TL and VL analysis of RODLD-C4E technique on Indian Pines dataset

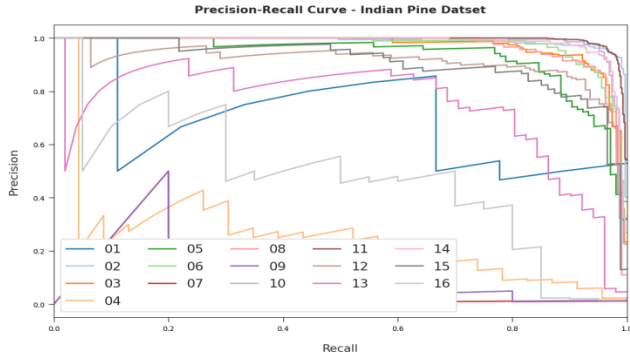


Figure 8. Precision-recall curve analysis of RODLD-C4E technique on Indian Pines dataset

A brief precision-recall examination of the RODLD-C4E model on Indian Pines dataset is portrayed in Figure 8. By observing the figure, it is noticed that the RODLD-C4E model has accomplished maximum precision-recall performance under all classes.

Figure 9 offers a detailed discussion of the comparative crop classification outcomes reported by the RODLD-C4E model on Indian Pines dataset (Li *et al.*, 2018; Zhou *et al.*, 2020). The experimental values indicated that the RODLD-C4E model has proficiently recognized all the class labels compared to other existing methods with maximum accuracy and kappa of 98.96% and 90.45% respectively.

Table 3. Result analysis of RODLD-C4E technique with several of measures on Salinas dataset

Class Label	Accuracy	Precision	Recall	Specificity	F-Score	Kappa Score
Category-01	99.73	96.18	96.40	99.86	96.29	-
Category-02	99.69	97.15	98.32	99.79	97.73	-
Category-03	99.75	96.14	97.02	99.86	96.58	-
Category-04	99.79	95.41	96.89	99.87	96.15	-
Category-05	99.65	95.95	97.05	99.78	96.50	-
Category-06	99.69	98.66	97.14	99.89	97.90	-
Category-07	99.73	97.60	98.22	99.83	97.91	-
Category-08	99.62	99.44	98.72	99.86	99.08	-
Category-09	99.68	98.62	98.68	99.81	98.65	-
Category-10	99.65	96.68	97.81	99.77	97.24	-
Category-11	99.76	94.09	92.83	99.89	93.45	-
Category-12	99.77	96.61	97.05	99.87	96.83	-
Category-13	99.71	95.05	88.48	99.92	91.65	-
Category-14	99.68	93.13	90.42	99.87	91.75	-
Category-15	99.71	98.57	99.25	99.78	98.91	-
Category-16	99.80	96.77	97.26	99.89	97.01	-
Average	99.71	96.63	96.35	99.85	96.48	97.45

Figure 10 illustrates the confusion matrix produced by the RODLD-C4E technique on 30% of TS data on Salinas dataset. The figure indicated that the RODLD-C4E approach has proficiently recognized 16 classes.

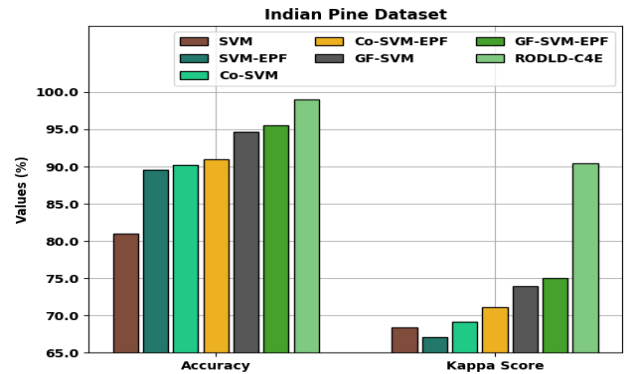


Figure 9. Comparative analysis of RODLD-C4E technique on Indian Pines dataset

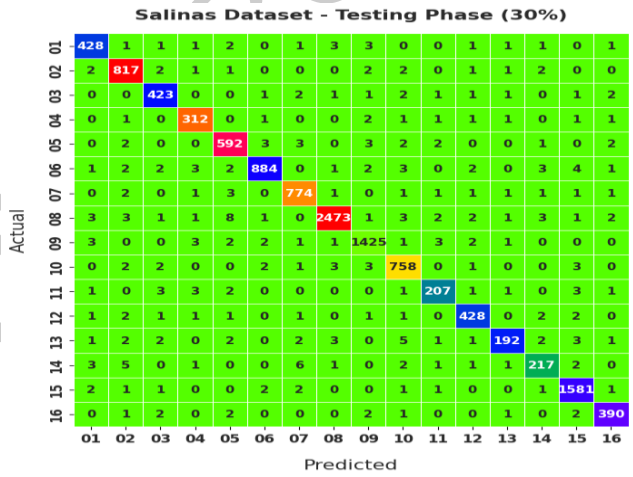


Figure 10. Confusion matrix of RODLD-C4E technique on 30% of TS data on Salinas dataset

Table 3 and Figure 11 give a detailed discussion of the crop classification outcomes reported by the RODLD-C4E model on Salinas dataset. The experimental values referred that the RODLD-C4E model has proficiently recognized all the class labels. For instance, with category 1, the RODLD-C4E model has provided $accu_y$, $prec_n$, $reca$, $spec_y$, and F_{score} of 99.73%, 96.18%, 96.40%, 99.86%, and 96.29% correspondingly. Also, with category 10, the RODLD-C4E technique has obtainable $accu_y$, $prec_n$, $reca$, $spec_y$, and F_{score} of 99.65%, 96.68%, 97.81%, 99.77%, and 97.24% correspondingly. At last, with category 16, the RODLD-C4E algorithm has provided $accu_y$, $prec_n$, $reca$, $spec_y$, and F_{score} of 99.80%, 96.77%, 97.26%, 99.89%, and 97.01% correspondingly.

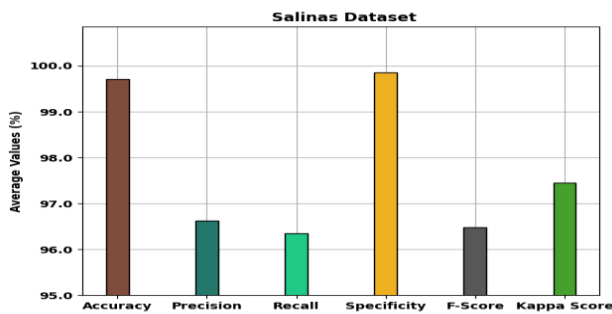


Figure 11. Result analysis of RODLD-C4E technique on Salinas dataset

The TA and VA attained by the RODLD-C4E model on Salinas dataset are portrayed in Figure 12. The experimental outcomes implied that the RODLD-C4E model has gained maximum values of TA and VA. In specific, the VA has appeared that superior to TA.

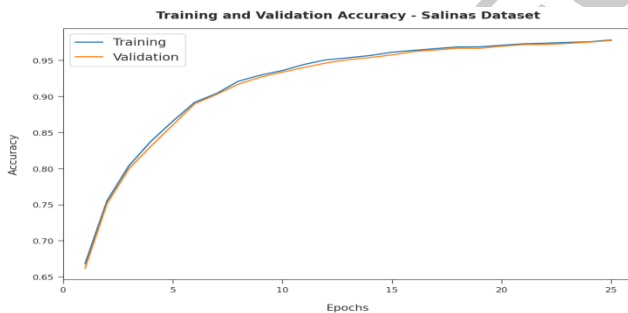


Figure 12. TA and VA analysis of RODLD-C4E technique on Salinas dataset

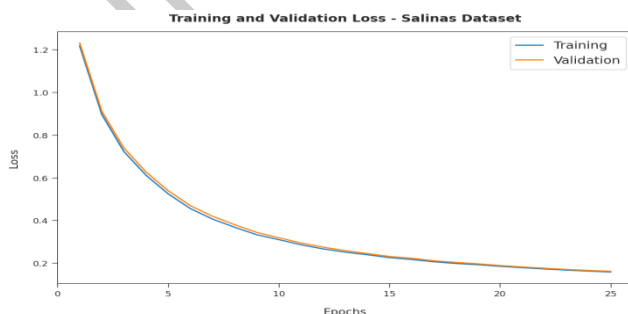


Figure 13. TL and VL analysis of RODLD-C4E technique on Salinas dataset

The TL and VL reached by the RODLD-C4E approach on Salinas dataset are recognized in Figure 13. The

experimental outcomes inferred that the RODLD-C4E model has accomplished least values of TL and VL. In specific, the VL is looked to be lesser than TL.

A brief precision-recall examination of the RODLD-C4E model on Salinas dataset is portrayed in Figure 14. By observing the figure, it can be noticed that the RODLD-C4E model has accomplished maximum precision-recall performance under all classes.

Figure 15 provides a detailed discussion of the comparative crop classification outcomes reported by the RODLD-C4E method on Salinas dataset. The experimental values exposed that the RODLD-C4E model has proficiently recognized all the class labels compared to other existing methods with maximal accuracy and kappa of 99.71% and 97.45% respectively.

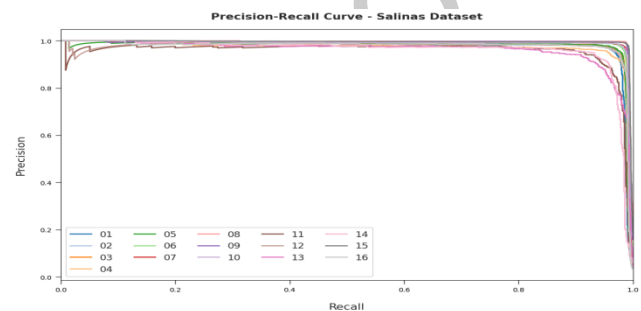


Figure 14. Precision-recall curve analysis of RODLD-C4E technique on Salinas dataset

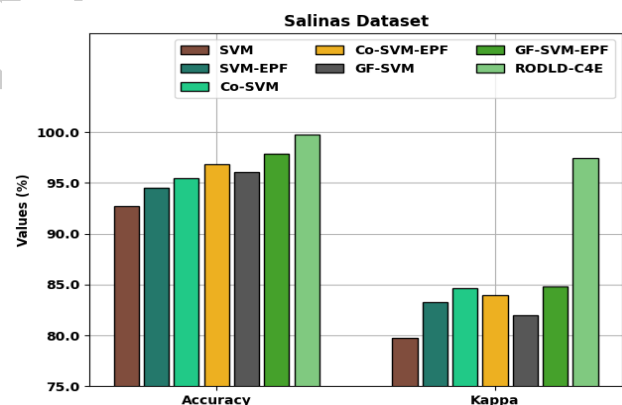


Figure 15. Comparative analysis of RODLD-C4E technique on Salinas dataset

Figure 16 reports the RMSE outcomes of the RODLD-C4E model with existing models on cross-validation and ground validation. The figure indicated that the RODLD-C4E model has accomplished lower values of RMSE under every aspect. For instance, with CV data, the RODLD-C4E model has offered reduced RMSE of 12.27 $\mu\text{g}\cdot\text{cm}^{-2}$ whereas the GPR-CBD, GPR-ABD, GPR-PAL, GPR-RSAL, and GPR models have obtained increased RMSE of 13.83, 15.19, 14.73, 14.75, and 16.93 $\mu\text{g}\cdot\text{cm}^{-2}$ respectively. At the same time, with GV data, the RODLD-C4E system has offered decreased RMSE of 12.36 $\mu\text{g}\cdot\text{cm}^{-2}$ whereas the GPR-CBD, GPR-ABD, GPR-PAL, GPR-RSAL, and GPR systems have obtained enhanced RMSE of 14.53, 16.44, 14.13, 13.17, and 31.98 $\mu\text{g}\cdot\text{cm}^{-2}$ correspondingly.

Figure 17 demonstrates the RRMSE outcomes of the RODLD-C4E method with existing models on cross-

validation and ground validation. The figure exposed that the RODLD-C4E model has accomplished lower values of RRMSE under every aspect. For instance, with CV data, the RODLD-C4E algorithm has accessible reduced RRMSE of 21.57% whereas the GPR-CBD, GPR-ABD, GPR-PAL, GPR-RSAL, and GPR approaches have reached enhanced RRMSE of 24.60%, 26.92%, 26.12%, 26.15%, and 30% correspondingly. Concurrently, with GV data, the RODLD-C4E model has obtainable reduced RRMSE of 12.69% whereas the GPR-CBD, GPR-ABD, GPR-PAL, GPR-RSAL, and GPR algorithms have obtained enhanced RRMSE of 25.44%, 28.78%, 24.74%, 23.06%, and 56% correspondingly.

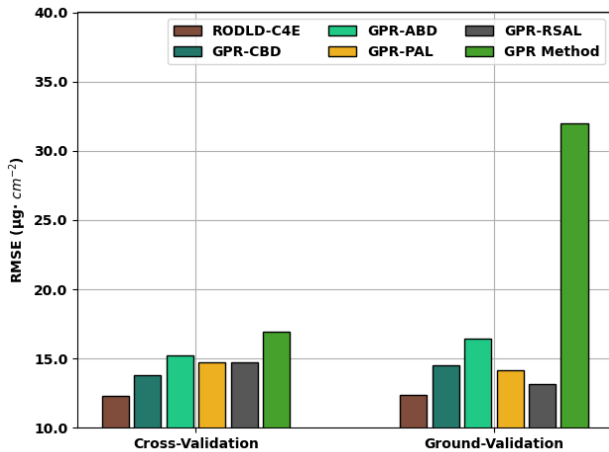


Figure 16. RMSE analysis of RODLD-C4E technique with existing algorithms

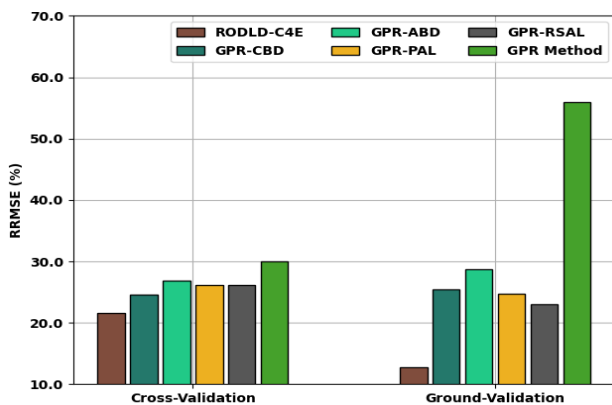


Figure 17. RRMSE analysis of RODLD-C4E technique with existing algorithms

From the detailed results and discussion, it is obvious that the RODLD-C4E model has resulted in enhanced outcomes over other models.

5. Conclusion

In this study, a new RODLD-C4E model was established to properly identify the crop type and chlorophyll content. The proposed RODLD-C4E model initially derives a RO algorithm with NASNetLarge model for feature extraction process. The utilization of RO algorithm enables to effectually adjust the hyperparameters of the

NasNetLarge model. In addition, the CGRU model is employed for crop type classification. At last, the DBN model is applied to estimate the chlorophyll content exists in the crop. To demonstrate the better performance of RODLD-C4E model, a wide ranging experimental analysis was implemented on benchmark dataset. The comparative analysis pointed out the better outcomes of the RODLD-C4E model under several aspects. Thus, the RODLD-C4E model can be exploited for effective crop classification and chlorophyll content estimation. In future, fusion of DL techniques can be employed to improve the classification performance.

References

- Brewer K., Clulow A., Sibanda M., Gokool S., Naiken V. and Mabhaudhi T. (2022). Predicting the Chlorophyll Content of Maize over Phenotyping as a Proxy for Crop Health in Smallholder Farming Systems. *Remote Sensing*, 14(3), 518.
- Denis A., Desclee B., Migdall S., Hansen H., Bach H., Ott P., Kouadio A.L. and Tychon B. (2020). Multispectral remote sensing as a tool to support organic crop certification: assessment of the discrimination level between organic and conventional maize. *Remote Sensing*, 13(1), 117.
- Denis A., Desclee B., Migdall S., Hansen H., Bach H., Ott P., Kouadio A.L. and Tychon B. (2021). Multispectral remote sensing as a tool to support organic crop certification: assessment of the discrimination level between organic and conventional maize. *Remote Sensing*, 13(1), 117.
- Garnot V.S.F., Landrieu L., Giordano S. and Chehata N. (2019). July. Time-space tradeoff in deep learning models for crop classification on satellite multi-spectral image time series. In *IGARSS 2019-2019 IEEE International Geoscience and Remote Sensing Symposium* (6247–6250). IEEE.
- Jia H., Peng X. and Lang C. (2021). Remora optimization algorithm. *Expert Systems with Applications*, 185, 115665.
- Kumar S. and Jayagopal P. (2021). Delineation of field boundary from multispectral satellite images through U-Net segmentation and template matching. *Ecological Informatics*, 64, 101370.
- Li C., Yang S.X., Yang Y., Gao H., Zhao J., Qu X., Wang Y., Yao D. and Gao J. (2018). Hyperspectral remote sensing image classification based on maximum overlap pooling convolutional neural network. *Sensors*, 18(10), 3587.
- Li H., Zhang C., Zhang S. and Atkinson P.M. (2019). A hybrid OSVM-OCNN method for crop classification from fine spatial resolution remotely sensed imagery. *Remote Sensing*, 11(20), 2370.
- Li Y., Zou L., Jiang L. and Zhou X. (2019). Fault diagnosis of rotating machinery based on combination of deep belief network and one-dimensional convolutional neural network. *IEEE Access*, 7, 165710–165723.
- Ma Q., Han W., Huang S., Dong S., Li G. and Chen H. (2021). Distinguishing Planting Structures of Different Complexity from UAV Multispectral Images. *Sensors*, 21(6), 1994.
- Moody D.I., Brumby S.P., Chartrand R., Keisler R., Longbotham N., Mertes C., Skillman S.W. and Warren M.S. (2017). May. Crop classification using temporal stacks of multispectral satellite imagery. In *Algorithms and Technologies for Multispectral, Hyperspectral, and Ultraspectral Imagery XXIII* (10198. 101980G). International Society for Optics and Photonics.

- Moriarty C., Cowley D.C., Wade T. and Nichol C.J. (2019). Deploying multispectral remote sensing for multi-temporal analysis of archaeological crop stress at Ravenshall, Fife, Scotland. *Archaeological Prospection*, 26(1), 33–46.
- Qi H., Wu Z., Zhang L., Li J., Zhou J., Jun Z. and Zhu B. (2021). Monitoring of peanut leaves chlorophyll content based on drone-based multispectral image feature extraction. *Computers and Electronics in Agriculture*, 187, 106292.
- Rußwurm M. and Korner M. (2017). Temporal vegetation modelling using long short-term memory networks for crop identification from medium-resolution multi-spectral satellite images. In *Proceedings of the IEEE Conference on Computer Vision and Pattern Recognition Workshops* (11–19).
- Senthilnath J., Kulkarni S., Benediktsson J.A. and Yang X.S. (2016). A novel approach for multispectral satellite image classification based on the bat algorithm. *IEEE Geoscience and Remote Sensing Letters*, 13(4), 599–603.
- Siesto G., Fernández-Sellers M. and Lozano-Tello A. (2021). Crop Classification of Satellite Imagery Using Synthetic Multitemporal and Multispectral Images in Convolutional Neural Networks. *Remote Sensing*, 13(17), 3378.
- Singhal G., Bansod B., Mathew L., Goswami J., Choudhury B.U. and Raju P.L.N. (2019). Chlorophyll estimation using multi-spectral unmanned aerial system based on machine learning techniques. *Remote Sensing Applications: Society and Environment*, 15, 100235.
- Singhal G., Bansod B., Mathew L., Goswami J., Choudhury B.U. and Raju P.L.N. (2019). Estimation of leaf chlorophyll concentration in turmeric (*Curcuma longa*) using high-resolution unmanned aerial vehicle imagery based on kernel ridge regression. *Journal of the Indian Society of Remote Sensing*, 47(7), 1111–1122.
- Thyagarajan K.K. and Vignesh T. (2019). Soft computing techniques for land use and land cover monitoring with multispectral remote sensing images: A review. *Archives of Computational Methods in Engineering*, 26(2), 275–301.
- Townsend P.A. and Walsh S.J. (2001). Remote sensing of forested wetlands: application of multitemporal and multispectral satellite imagery to determine plant community composition and structure in southeastern USA. *Plant Ecology*, 157(2)129–149.
- Ünal Y., Öztürk Ş., Dudak M.N. and Ekici M. (2022). Comparison of Current Convolutional Neural Network Architectures for Classification of Damaged and Undamaged Cars. In *Advances in Deep Learning, Artificial Intelligence and Robotics* (141–149). Springer, Cham.
- Wang L., Wang J., Liu Z., Zhu J. and Qin F. (2022). Evaluation of a deep-learning model for multispectral remote sensing of land use and crop classification. *The Crop Journal*.
- Xu C., Shen J., Du X. and Zhang F. (2018). An intrusion detection system using a deep neural network with gated recurrent units. *IEEE Access*, 6, 48697–48707.
- Yang D., Zhao J., Lan Y., Wen Y., Pan F., Cao D., Hu C. and Guo J. (2021). Research on farmland crop classification based on UAV multispectral remote sensing images. *International Journal of Precision Agricultural Aviation*, 4(1).
- Zhou X., Zhang J., Chen D., Huang Y., Kong W., Yuan L., Ye H. and Huang W. (2020). Assessment of leaf chlorophyll content models for winter wheat using Landsat-8 multispectral remote sensing data. *Remote Sensing*, 12(16), 2574.
- Zhou Z., Li S. and Shao Y. (2018). July. Crops classification from sentinel-2A multi-spectral remote sensing images based on convolutional neural networks. In *IGARSS 2018-2018 IEEE International Geoscience and Remote Sensing Symposium* (5300–5303). IEEE.